WILEY-VCH

DOI: 10.1002/((please add manuscript number))
Article type: Communication

Bionic Detectors Based on Low-Bandgap Inorganic Perovskite for Selective NIR-I Photon Detection and Imaging

Fei Cao,[#] Jingde Chen, [#] Dejian Yu, [#] Shu Wang, Xiaobao Xu, Jiaxin Liu, Zeyao Han, Bo Huang, Yu Gu, Kwang Leong Choy, Haibo Zeng**

((Optional Dedication))

Dr. F. Cao, Dr. D. Yu, Prof. X. Xu, Dr. J. Liu, Dr. Z. Han, B. Huang, Prof. Y. Gu, Prof. H. Zeng
Institute of Optoelectronics & Nanomaterials, MIIT Key Laboratory of Advanced Display Materials and Devices, School of Materials Science and Engineering, Nanjing University of Science and Technology, Nanjing 210094, China.

Prof. J. Chen, Miss. S. Wang
Jiangsu Key Laboratory for Carbon-Based Functional Materials & Devices, Institute of Functional Nano & Soft Materials (FUNSOM), Soochow University, Suzhou, 215123, Jiangsu, PR China

Prof. K. L. Choy
Institute for Materials Discovery, University College London, Roberts Building, Malet Place, London, WC1E 7JE, United Kingdom

[#] F. Cao, J. Chen, and D. Yu contributed equally to this work

* E-mail: xiaobaoxu@njust.edu.cn, zeng.haibo@njust.edu.cn

Keywords: halide perovskite, bionic photodetector, NIR-I detection, narrowband detection, fluorescence imaging

ABSTRACT: Fluorescence imaging with photodetectors (PDs) toward near-infrared I (NIR-I) photons (700 nm~ 900 nm), the so-called “optical window” in organisms, has provided an important path for tracing biological processes in vivo. With both excitation photons and fluorescence photons in this narrow range, a stringent requirement arises that the fluorescence signal should be efficiently differentiated for

effective sensing, which cannot be fulfilled by common PDs with a broadband response such as Si-based PDs. In this work, inspired by the compound eyes of butterflies, delicate optical microcavities are designed to develop a series of bionic PDs with selective response to NIR-I photons, the merits of a narrowband response with full width at half maximum (FWHM) of <50 nm and tunability to cover the NIR-I range are highlighted. Inorganic halide perovskite $CsPb_{0.5}Sn_{0.5}I_3$ is chosen as the photoactive layer with comprehensive bandgap and film engineering. As a result, these bionic PDs offer a signal/noise ratio of ~10^6, a large bandwidth of 543 KHz and an ultralow detection limit of 0.33 nW. Meanwhile, the peak responsivity (R) and detectivity (D*) reach up to 270 mA/W and 5.4×10^{14} Jones, respectively. Finally, proof-of-concept NIR-I imaging using the PDs is demonstrated to show their great promise in real-life application.

Near-infrared photodetector (NIR PDs) towards distinct photon signal from 700 nm~ 900 nm (NIR-I) have attracted much attention in the past decades due to their tremendous potential in medical instruments.[1] Benefitting from merits including low photodamage to biological sample, deep tissue penetration, and minimum interference from background autofluorescence in living biosystems, the detection and imaging of fluorescence photons in this range have been regarded as a powerful real-time technique for medical diagnosis, surgery or therapy.[2] Up to now, the realization of photon sensing in this characteristic NIR-I region mainly relies on inorganic narrow-bandgap

materials. For example, gallium arsenide, silicon, lead selenide and indium gallium arsenide have been intensely explored as the photoactive layer in NIR PDs.[2b, 3] Nevertheless, the fabrication processes including alloying, doping, etching, epitaxy and so on in these inorganic narrow-bandgap materials are very complicated and costly. What's worse, with both excitation photons and fluorescence photons in the narrow NIR-I range, bandgap-determined broadband response in these NIR PDs cripples them in selectively sensing the characteristic NIR-I fluorescence, because noise from excitation photons cannot be effectively excluded. Challengingly, novel PDs that respond to specific narrowband NIR-I photons are highly demandable.

Due to favorable attributes including facile processability, tunable optical bandgap, high light-harvesting coefficient and decent charge carrier mobility, the prosperous halide perovskite (HP) materials show the promise of developing low-cost high-performance PDs.[4] Desirably, Pb-Sn binary low-bandgap HPs offer spectral response to NIR region that covers NIR-I photons,[5] and narrowband PDs have been proposed with the mechanism of modulating surface-charge-recombination and intermolecular-charge-transfer.[6] Unfortunately, the realization of such narrowband characteristic NIR-I response comes with a sacrifice in device performance, which results in compromised responsivity and detectivity in PDs.[7]

Nature is fantastic as it offers many examples of compact, energy-efficient, adaptable and intelligent imaging systems. For example, the antifogging functionality of mosquito eyes give researchers the hint to invent an anti-fogging artificial compound-eye structure;[8] The colors originating from the special hierarchical structures found in

peacock feathers inspired scientists to develop a high-resolution multicoloured patterning technique, which can artificially achieve structural colors within seconds by using a single material and flexible photonic crystals;[9] Even a puny animal like butterfly shows more exquisite perception of the environment than human beings,[2b] the compound eyes of butterflies can recognize objects with filtrated light in specific bands, this inspires us to mimic such structure to construct light-selective PDs.

In this work, equipped with delicate optical microcavities enlightened by the compound eyes of butterfly, a series of bionic PDs that selectively respond to NIR-I photons are introduced. The microcavities are constructed with LiF (n=1.33, n is refractive index) and NPB (N,N'-Bis(naphthalen-1-yl)-N,N'-bis(phenyl)benzidine, n=2.1) that act as tapetum cells in the compound eyes of butterfly. Fully-inorganic $CsPb_{0.5}Sn_{0.5}I_3$ HP is adopted as the photoactive layer, the band edge extends to 900 nm to cover the NIR-I range. As a result, the PDs exhibit tunable narrowband (full width at half maxium (FWHM) <50 nm) photon sensing in the NIR-I window, therefore affording high-efficiency detection of characteristic fluorescent signals by excluding the noise from excitation photons. Besides, Comprehensive composition and film engineering are carried out to boost the performance of the PDs. The rapid response with a bandwidth of 543 KHz and an ultralow detection limit of 0.33 nW certify the capability of real-time and high-resolution sensing. All the key figure of merits including a noise current less than 10^{-13} A $Hz^{-1/2}$ and a detectivity (D*) of ~10^{14} Jones ensure efficient detection and imaging in the biomedical field, as is demonstrated in a self-built imaging system.

The typical light absorption spectrum in organism is shown in **Figure 1**a. The hemoglobin, tissues and lipid account for major absorption of visible photons from 400 nm to 700 nm, while water shows significant absorption of photons with >900 nm wavelength.[10] In contrast, light signal in the range of 700 nm~900 nm offers strong penetrability in living bodies (ca. 0.5 mm to cm), therefore is coded as "the optical window" for *in vivo* imaging.[1a, 1c] Under excitation of NIR-I photons, the infrared fluorescent dyes that anchor on tumors or virus cells emit down-converted NIR-I fluorescence, which is then sensed and mapped by PDs.[2a, 2c, 2d] Especially, PDs responding to the narrowband characteristic NIR-I fluorescent signal as well as excluding NIR-I excitation photons can efficiently heighten the sensing and imaging performance with a larger signal/noise ratio.

To meet this requirement, we turn our attention to vision systems with such function in nature. Here, the colorful butterflies give us the inspiration, since the compound eyes of Morpho butterflies endow them with remarkable sensing ability to recognize ultraviolet, visible and NIR photons with selective enhancement in different ommatidia.[2b] Figure 1b shows the structure of a typical ommatidium in butterflies, there are many alternating layers of air and cytoplasm (called tapetum cells) at the proximal end of the rhabdom within each ommatidium, these alternating layers act as optical mircocavities to selectively allow through photons of specific wavelength.[2b] The resolution of different photons can be accomplished by adjusting the alternating layers in different ommatidia. Inspired by this, we propose bionic narrowband NIR-I PDs that imitate the microstructure of butterfly's compound eyes. Figure 1c presents

the schematic diagram of the proposed bionic PD architecture. At the top, there are microcavities consisting of dielectric media layers that act as the tapetum cells. In the bottom there is a broadband PD that responds in the NIR range (the role of rhabdom), the overall device can achieve enhanced detection of specific narrowband NIR-I photons similar to the ommatidia of butterflies.

Bionic optical microcavity is constructed as shown in **Figure 2**a, the optical microcavity composes of alternating LiF (n=1.33)/NPB (N,N'-Bis(naphthalen-1-yl)-N,N'-bis(phenyl)benzidine, n=2.1) layers to simulate the tapetum cells in the eyes of butterflies. The optical thickness of each layer is designed to be a quarter of the target wavelength. Take the specific wavelength of 850 as an example, the thickness of LiF and NPB are set as 158 nm and 116 nm, respectively. The peak wavelength of the transmission light can be modulated via adjusting the thickness of dielectric media to cover the range of 700 nm-900 nm. Figure 2b displays the simulation of optical field distribution in the proposed tunable microcavities, clearly, the transmission spectra are narrowed in such microcavities. Corresponding transmittance spectra are shown in **Figure S**1. These results confirm that PDs selectively respond to NIR-I light can be constructed with such bionic microcavities.

Then, PDs with effective response in the NIR-I band, atop which the above functional microcavities are equipped, should be built. For the application of real-time imaging, photoactive materials are the key with the requirement of fast response, high resolution and low detection limit. Recently, HPs emerged with facile solution synthesis, low cost, and exceptional semiconducting properties,[11] especially, fully-inorganic HPs enjoy

comparable semiconducting properties with the most-widely studied hybrid counterparts but much better stability,[12] therefore are selected as the photoactive layer in the PDs here. However, the intrinsic photoresponse of $CsPbI_3$ film cuts only at 700 nm~750 nm, which misses the NIR-I window.[13] Fortunately, Sn alloying can be carried out to engineer its bandgap to fully cover the NIR-I range.[14] **Figure 3**a shows the ultraviolet-visible (UV−vis) absorption spectra of a series of $CsPb_xSn_{1-x}I_3$ films. It is noteworthy that the absorption of black-phase $CsPbI_3$ is not offered due to its spontaneous transition to non-HP phase at room temperature,[15] but the phase stability is greatly improved with the incorporation of Sn, which can be ascribed to the intensive strain in lattice caused by the mismatch of radius between Pb 1.19 Å) and Sn (1.15 Å).[16] Indeed, a redshift of absorption onset is observed as the Sn concentration increases, the absorption at 900 nm is obtained in $CsPb_{0.5}Sn_{0.5}I_3$, which meets the requirement of bio-marker fluorescence detection in the NIR-I range.

However, when Sn is incorporated, the morphology of the film becomes worse because of the different crystallization rates in Pb- and Sn- HPs.[5a] The grain size and film coverage of $CsPb_xSn_{1-x}I_3$ films (x = 0 ~1) are characterized by atomic force microscope (AFM) as shown in **Figure S**2. Clearly, the $CsPbI_3$ and $CsSnI_3$ thin films (x=1 and 0) consist of large grains and few pinholes, but in Pb-Sn ($CsPb_{0.7}Sn_{0.3}I_3$ and $CsPb_{0.5}Sn_{0.5}I_3$) alloyed films, the grain size becomes non-uniform and less dense with more pinholes, which compromise the performance of subsequent PDs.[17] To solve this problem, a small amount of two-dimensional (2D) HP is added to improve the quality of thin films. Here, 5% $(PEA)_2Pb_{0.5}Sn_{0.5}I_4$ was adopted. Figure 3b gives the top view

SEM images of the HP films. Many pinholes were observed in the pristine $CsPb_{0.5}Sn_{0.5}I_3$ film, as is in good agreement with the above AFM characterization. In contrast, the film obviously becomes uniform and dense after the incorporation of 2D HPs. This pinhole-free film can efficiently promote the PD performance by suppressing oxygen and moisture penetration that cause undesirable Sn^{2+} oxidation.[18] The charge carrier dynamics of the thin films on glass is the investigated using photoluminescence (PL) decay transient spectra. As shown in Figure 3c, the time constants (τ) associated with the lifetime of charge carrier are 6.6 ns and 13.8 ns in the pristine $CsPb_{0.5}Sn_{0.5}I_3$ film and the film with 5% $(PEA)_2Pb_{0.5}Sn_{0.5}I_4$ additive, respectively. This greatly prolonged charge carrier lifetime implies a decrease of defects. **Figure S**3 shows the measured density of defect states in devices from chemical capacitance with electrochemical impedance technique in darkness, consistently, a suppressed defect density upon increasing $(PEA)_2Pb_{0.5}Sn_{0.5}I_4$ content is unambiguously unveiled. **Figure S**4 displays the current-voltage (J-V) curves for the PDs under simulated AM 1.5G irradiation (100 mW cm^{-2}), a good short-circuit photocurrent of ~22 mA cm^{-2} is achieved, which suggests good performance as photodiodes.

Figure 3d provides the X-ray diffraction (XRD) patterns of the HP films. The sharp characteristic peaks well reveal the formation of highly crystalline 3D HPs with the 2D HP additive. Referring to previous reports, incorporating trace amount of 2D HP can enhance the orientation preference.[19] Indeed, Figure 3e shows the corresponding 2D XRD pattern of the films. In pure $CsPb_{0.5}Sn_{0.5}I_3$, the pattern shows Debye−Scherrer rings with an isotropical intensity distribution, which indicates complete randomness in

the orientation of grains. With the 2D HP additive, a series of Bragg spots appear in place of the original diffraction rings, implying that crystal grains grow along a particular orientation. The consecutive orientation evolution upon increasing amount of additive is shown in **Figure S**5. Finally, sharp and discrete Bragg spots are observed in the 2D:3D = 1:10 sample. To clarify the effect of orientation on charge transport, we further conducted I-V tests on the engineered HP films[20]. As shown in **Figure S**6, we characterized the film along two directions: 1) one is the out-of-plane direction (**Figure S**6a), the electrodes are on the two horizontal sides of the film to test the horizontal carrier transport. The I-V curves are shown in **Figure S**6c, the decreasing current indicates that carrier mobility gradually reduces along the out-of-plane direction as the 2D HP content increases; 2) While in the other case (namely along the in-plane direction, **Figure S6**b), the I-V curves in **Figure S**6d reveal unchanged current upon increased 2D HP content. The in-plane direction is the working direction of the PDs, and the I-V result points out that the 2D HP additive preserves the good charge carrier transport while improving the film quality.

After comprehensive composition and film engineering to obtain high-quality HP films for PDs, the bionics-inspired microcavities are mounted onto them to experimentally demonstrate the selective light response. Three types of PDs with transmission peaks of 800 nm, 850 nm and 900 nm (labeled as PD-1, PD-2 and PD-3 for in the following, respectively) are fabricated for characterizations. **Figure 4**a presents the normalized monochromatic external quantum efficiency (EQE) of as-fabricated bionic PDs toward specific NIR-I photons at zero bias, it shows that the

response spectra in the NIR-I range are effectively narrowed into a unimodal spectral line (FWHM <25 nm). The narrow response to NIR-I photons is desirable in biomedical fluorescence imaging, which ensures effective differentiation of the NIR-I fluorescence from excitation photons.[21] According to the equation:

$$R=EQE*e/h\nu \qquad (1)$$

the peak responsivity (*R*) is estimated to be 0.26 A W^{-1}, 0.27 A W^{-1} and 0.04 A W^{-1} in PD-1, PD-2 and PD-3, respectively (**Figure S**7). Figure 4b displays the dark current and the photocurrent under flat-spectrum white light (AM 1.5 illumination) of NIR-I PDs in short-circuit condition. A small dark current of 5.28×10^{-7} mA cm^{-2} is observed, while the photocurrent of 1.48 mA cm^{-2}, 0.68 mA cm^{-2} and 0.12 mA cm^{-2} were obtained in the three NIR-I PDs peaked at 800 nm, 850 nm and 900 nm, respectively. A large signal-noise ratio of ~10^6 is obtained, the high ratio is essential for precise detection of weak signals.

To further clarify the capability of resolving weak light in our NIR-I PDs, the photocurrent response under illumination with various intensities was conducted, which is measured with PD-1. Figure 4c shows the linear dynamic range (LDR) with irradiated photon power less than 1 microwatt. Intriguingly, the PDs show linear response limit down to 0.33 nW. In this linear range the variation in light signal intensity can be precisely translated into electricity change, which provides a solid base for the technology of faint fluorescence imaging. And to realize real-time resolution, fast

response rate is also required. Here we evaluate the response rate with representative response bandwidth based on the photo-switching behaviour of the PDs under different on/off switching frequencies of the light source. **Figure S**8 is the I-t response curves in function of light switching frequency. As shown in Figure 4d, the representative -3dB bandwidth is 543 KHz. The response speed is much faster than the newest refresh speed in typical electronic devices (120 Hz). It is noteworthy that the active area in our NIR-I PDs is 0.2 cm^2, and this response speed is expected to be further improved if the active area is pixelated to microscale.

We further investigated the noise current of the device PD-1, which was obtained by a fast Fourier transform (FFT) calculation from dark current-time characterization, the result is presented in Figure 4e. The noise is estimated to be $1.65*10^{-13}$ A $Hz^{-1/2}$ at 1Hz, and the white noise dominates above 2 Hz instead of 1/f noise. Then the noise equivalent power (NEP) is calculated according to the following formula:

$$NEP= i_n/R \qquad (2)$$

where R is the responsivity and i_n is the measured noise current. The calculated NEP of the NIR PD is plotted in **Figure S**9, a small value of 0.83 pW $Hz^{-1/2}$ is achieved at 850 nm. Furtherly, detectivity (D*) can be obtained according to the following equation:

$$D^*=(A\times f_{-3dB})^{1/2}/NEP \qquad (3)$$

where A is the active area. The calculated result is plotted in Figure 4f. The peak D* values in PD-1, PD-2 and PD-3 are ~5.25×10^{14} Jones, ~5.42×10^{14} and ~8.89×10^{13} Jones, respectively. Notably, these values are comparable to those of the highly sensitive commercial Si PDs, which suggests their potential for dim light detection.[22]

After confirming the superior performance, the capability of NIR-I fluorescence imaging in the bionic narrowband NIR-I PDs was further demonstrated. The set-up is shown in **Figure 5**a, a hollowed-out mask of letter "N" was placed between the NIR light source and the PD. Our PD was used as the light-sensitive component and scans in both vertical and horizontal directions for fluorescence mapping. Herein, the bionic narrowband PDs-2 with peak response of 850 nm was taken as the platform. As shown in Figure 5b, no clear contrast can be obtained with a 750 nm emitting source, but a discernible figure dark "N" was observed with an 850 nm light source (Figure 5c). The response to different photons confirms selectivity to desirable signal in the bionic PDs. Notably, the obvious intensity variation in the mapping pattern between the upper part and the bottom part is attributed to an imperfect perpendicularity to light in the scanning plane of PD, this also points out a high resolving capability that even small changes in light intensity can be detected.

In summary, with all-inorganic HPs $CsPb_{0.5}Sn_{0.5}I_3$ as the photoactive layer and microcavity that mimicking the tapetum cells in butterfly′s compound eyes, we obtained a series of bionic NIR PDs that selectively respond to narrowband NIR-I photons. The FWHM in the as-fabricated PDs is less than 50 nm, while the bandwidth and detection limit reach 543 KHz and 0.33 nW, respectively. With the low noise

current of 1.65 ×10-^{13} A $Hz^{-1/2}$, the peak detectivity (D*) reaches up to 5.4×10^{14} Jones. For the detection and imaging of NIR-I photons, these bionic PDs present three prominent advantages of 1) signal selectivity; 2) material-independent functionality; 3) facile array fabrication. We believe this work paves the way to advanced technologies of biomedical fluorescence detection.

Experimental Section

Chemicals: All chemicals and reagents were purchased from Sigma-Aldrich without further purification. All solutions were filtered with a 0.45 μm PTFE (polytetrafluoroethylene) filter prior to use.

Device Fabrication: The fabrication of PD-1, PD-2 and PD-3 are all the same despite the thickness of the optical microcavities, the optimal $CsPb_{0.5}Sn_{0.5}I_3$ was chosen as the active layer to fabricate the NIR narrowband PDs. ITO glass was first cleaned by ultrasonication with detergent, deionized water, acetone, and isopropanol in sequence for 10 mins, respectively. Then, the substrates were dried by nitrogen flow and treated with ultraviolet–ozone for 20 mins before deposition of PEDOT: PSS. The PEDOT: PSS (Al 4083) solution was spin-coated onto the cleaned ITO glass at 5000 rpm for 30 s and annealed at 150 °C for 10 min in air. To prepare the precursor solution of $CsPb_{0.5}Sn_{0.5}I_3$ perovskite, CsI (259.8 mg), PbI_2 (230.5 mg), SnI_2 (186 mg) and SnF_2 (8 mg) were dissolved in a mixed solvent of dimethylformamide (DMF; 700 μL) and dimethylsulfoxide (DMSO; 300 μL). For the treated films, a small quantity of $PEA_2Pb_{0.5}Sn_{0.5}I_4$ precursors (24.9 mg PEAI, 11.5 mg PbI_2 and 9.3 mg SnI_2 in the 5%

addition 2D sample) were added into the precursor. Afterward, 35 μL of the perovskite precursor was dipped onto the PEDOT: PSS layer and spin-coated at 5000 rpm for 35 s in the glove box. Toluene (700 μL) was dripped in situ onto the substrate at the tenth second. After that, the obtained perovskite films were annealed at 100 °C for 3 mins. PCBM solution (20 mg mL^{-1} in chlorobenzene) was then spin-coated onto the perovskite film at 2000 rpm for 30 s. Finally, Ag electrode with a thickness of 120 nm was evaporated under high vacuum (< 2×10^{-6} torr). After the preparetion of common photodetector, a microcavity was constructed on the back to realize a bionic narrow-band photodetector by high-vaccum thermal evaporation, the chamber pressure is 2×10^{-6} torr. LiF and NPB films were deposited in sequence with a deposition rate of 8 Å/s and 10 Å/s, respectively, and the thickness was monitored by film thickness gauge. For PD-1, the NPB layer is 109 nm and LiF is 148 nm, respectively, they were deposited on the back of the glass substrate with the stacking order of $NPB/(LiF/NPB)^5/LiF/LiF/(NPB/LiF)^5NPB$. The thicknesses of the NPB layer and the LiF layer are reset to 116 nm/158 nm in PD-2, and 123/167 nm in PD-3.

Characterization*:* XRD was measured by an X-ray diffractometer (Bruker F8 Focus Powder for regular XRD and Bruker D8 Discover 2-D XRD for refined XRD). SEM images were obtained by FEI Sirion with an operating voltage of 5 kV. The absorption spectra were measured by a SHIMADZU UV-3600 UV-VIS-NIR spectrophotometer. The PL decay measurement was conducted with an IR detector (id 220-FR-MMF, id Quatique SA Geneva/Switzerland). Electronic impedance spectroscopy (EIS) was measured using electrochemistry workstation (Zennium E4) from Zahner. The J–V curves

were recorded by a Keithley 2400 Source measurement unit; a 450 W xenon lamp was used to produce light; and the light intensity of (100 mW cm^{-2}) was calibrated by a standard Si photodiode detector. The EQE spectra were measured by a joint system of a monochromated 450 W xenon lamp (Oriel) and a sourcemeter (Keithley 2400), which was calculated using a calibrated Si photodiode (OSI-Optoelectronics).

Noise Current Measurement*:* The noise current was extracted from the dark current, which was recorded by a sourcemeter (Keithley 6430 with Remote PreAmp using four-wire sense connections). A fast Fourier transform was adopted for calculation.

Supporting Information

Supporting Information is available from the Wiley Online Library or from the author.

Acknowledgements

F. Cao, J. Chen, and D. Yu contributed equally to this work. This work was financially supported by the Natural Science Foundation of Jiangsu Province (BK20190443, BK20160815), Young Elite Scientists Sponsorship Program by Jiangsu CAST (JS19TJGC132574), Fundamental Research Funds for the Central Universities (30919011299, 30919011298), National Key R&D Program of China (no. 2017YFA0305500), the National Natural Science Foundation of China (no. 11604152, 51672132).

Received: ((will be filled in by the editorial staff))
Revised: ((will be filled in by the editorial staff))
Published online: ((will be filled in by the editorial staff))

References

[1] a) T. Jin, F. Fujii, Y. Komai, J. Seki, A. Seiyama, Y. Yoshioka, *Int. J. Mol. Sci.* **2008**, *9*; b) P.G. Drummen, *Int. J. Mol. Sci.* **2010**, *11*; c) R. Weissleder, *Nat. Biotechnol.* **2001**, *19*, 316-317.

[2] a) S. Zhu, Z. Hu, R. Tian, B.C. Yung, Q. Yang, S. Zhao, D.O. Kiesewetter, G. Niu, H. Sun, A.L. Antaris, X. Chen, *Adv. Mater.* **2018**, *30*, 1802546; b) M. Garcia, C. Edmiston, T. York, R. Marinov, S. Mondal, N. Zhu, G.P. Sudlow, W.J. Akers, J. Margenthaler, S. Achilefu, R. Liang, M.A. Zayed, M.Y. Pepino, V. Gruev, *Optica* **2018**, *5*, 413-422; c) W. Zhu, C. Chu, S. Kuddannaya, Y. Yuan, P. Walczak, A. Singh, X. Song, J.W.M. Bulte, *Adv. Funct. Mater.* **2019**, *0*, 1903753; d) H.-W. Liu, X.-X. Hu, K. Li, Y. Liu, Q. Rong, L. Zhu, L. Yuan, F.-L. Qu, X.-B. Zhang, W. Tan, *Chem. Sci.* **2017**, *8*, 7689-7695.

[3] a) R. Yousefi, M.R. Mahmoudian, A. Sa´aedi, M. Cheraghizade, F. Jamali-Sheini, M. Azarang, *Ceram. Int.* **2016**, *42*, 15209-15216; b) G. Wu, R. Fu, J. Chen, W. Yang, J. Ren, X. Guo, Z. Ni, X. Pi, C.-Z. Li, H. Li, H. Chen, *Small* **2018**, *14*, 1802349; c) K.H. Hendriks, W. Li, M.M. Wienk, R.A.J. Janssen, *J. Am. Chem. Soc.* **2014**, *136*, 12130-12136; d) Z. Zheng, L. Gan, J. Zhang, F. Zhuge, T. Zhai, *Adv. Sci.* **2017**, *4*, 1600316.

[4] a) L. Gu, Z. Fan, *Light-Sci. Appl.* **2017**, *6*, e17090; b) Y.-C. Zhao, W.-K. Zhou, X. Zhou, K.-H. Liu, D.-P. Yu, Q. Zhao, *Light-Sci. Appl.* **2017**, *6*, e16243; c) C. Xie, P. You, Z. Liu, L. Li, F. Yan, *Light-Sci. Appl.* **2017**, *6*, e17023; d) F. Cao, D. Yu, X. Li, Y. Zhu, Z. Sun, Y. Shen, Y. Wu, Y. Wei, H. Zeng, *J. Mater. Chem. C* **2017**, *5*, 7441-7445; e) T. Zhang, J. Wu, P. Zhang, W. Ahmad, Y. Wang, M. Alqahtani, H. Chen, C. Gao, Z. D. Chen, Z. Wang, S. Li, *Adv. Opt. Mater*. **2018**, 6, 1701341; g) M.I. Saidaminov, V. Adinolfi, R. Comin, A.L. Abdelhady, W. Peng, I. Dursun, M. Yuan, S. Hoogland, E.H. Sargent, O.M. Bakr, *Nat. Commun.* **2015**, *6*; f) X. Hu, X.

Zhang, L. Liang, J. Bao, S. Li, W. Yang, Y. Xie, *Adv. Func. Mater.* **2014**, *24*, 7373-7380.

[5] a) W. Liao, D. Zhao, Y. Yu, N. Shrestha, K. Ghimire, C.R. Grice, C. Wang, Y. Xiao, A.J. Cimaroli, R.J. Ellingson, N.J. Podraza, K. Zhu, R.-G. Xiong, Y. Yan, *J. Am. Chem. Soc.* **2016**, *138*, 12360-12363; b) D. Chi, S. Huang, M. Zhang, S. Mu, Y. Zhao, Y. Chen, J. You, *Adv. Func. Mater.* **2018**, *28*, 1804603; c) B. Zhao, M. Abdi-Jalebi, M. Tabachnyk, H. Glass, V.S. Kamboj, W. Nie, A.J. Pearson, Y. Puttisong, K.C. Gödel, H.E. Beere, D.A. Ritchie, A.D. Mohite, S.E. Dutton, R.H. Friend, A. Sadhanala, *Adv. Mater.* **2017**, *29*, 1604744.

[6] a) W. Wang, F. Zhang, M. Du, L. Li, M. Zhang, K. Wang, Y. Wang, B. Hu, Y. Fang, J. Huang, *Nano Lett.* **2017**, *17*, 1995-2002; b) B. Siegmund, A. Mischok, J. Benduhn, O. Zeika, S. Ullbrich, F. Nehm, M. Böhm, D. Spoltore, H. Fröb, C. Körner, K. Leo, K. Vandewal, *Nat. Commun.* **2017**, *8*, 15421; c) Y. Fang, Q. Dong, Y. Shao, Y. Yuan, J. Huang, *Nat. Photonics* **2015**, *9*, 679-686.

[7] J. Xue, Z. Zhu, X. Xu, Y. Gu, S. Wang, L. Xu, Y. Zou, J. Song, H. Zeng, Q. Chen, *Nano Lett.* **2018**, *18*, 7628-7634.

[8] X. Gao, X. Yan, X. Yao, L. Xu, K. Zhang, J. Zhang, B. Yang, L. Jiang, *Adv. Mater.* **2007**, *19*, 2213-2217.

[9] H. Kim, J. Ge, J. Kim, S.-e. Choi, H. Lee, H. Lee, W. Park, Y. Yin, S. Kwon, *Nat. Photonics* **2009**, *3*, 534.

[10] S. Luo, E. Zhang, Y. Su, T. Cheng, C. Shi, *Biomaterials* **2011**, *32*, 7127-7138.

[11] a) M.A. Green, A. Ho-Baillie, H.J. Snaith, *Nat. Photonics* **2014**, *8*, 506-514; b) G. Xing, N. Mathews, S. Sun, S.S. Lim, Y.M. Lam, M. Grätzel, S. Mhaisalkar, T.C. Sum, *Science* **2013**, *342*, 344-347; c) W.-J. Yin, T. Shi, Y. Yan, *Adv. Mater.* **2014**, *26*, 4653-4658; d) C.S. Ponseca, T.J. Savenije, M. Abdellah, K. Zheng, A. Yartsev, T. Pascher, T. Harlang, P. Chabera, T. Pullerits, A. Stepanov, J.-P. Wolf, V. Sundström, *J. Am. Chem. Soc.* **2014**, *136*, 5189-5192; e) Q. Dong, Y. Fang, Y. Shao, P. Mulligan, J. Qiu, L. Cao, J. Huang, *Science* **2015**, *347*, 967-970; f) Y. Bi, E.M. Hutter, Y. Fang, Q. Dong, J. Huang, T.J. Savenije, *J. Phys. Chem. Lett.* **2016**, *7*, 923-928; g) E. Alarousu, A.M. El-Zohry, J. Yin, A.A. Zhumekenov, C. Yang, E. Alhabshi, I. Gereige, A. AlSaggaf, A.V. Malko, O.M. Bakr, O.F. Mohammed, *J. Phys. Chem. Lett.* **2017**, 4386-4390.

[12] a) G.R. Yettapu, D. Talukdar, S. Sarkar, A. Swarnkar, A. Nag, P. Ghosh, P. Mandal, *Nano Lett.* **2016**, *16*, 4838-4848; b) C.C. Stoumpos, C.D. Malliakas, J.A. Peters, Z. Liu, M. Sebastian, J. Im, T.C. Chasapis, A.C. Wibowo, D.Y. Chung, A.J. Freeman, B.W. Wessels, M.G. Kanatzidis, *Cryst. Growth Des.* **2013**, *13*, 2722-2727; c) T. Zhang, F. Wang, P. Zhang, Y. Wang, H. Chen, J. Li, J. Wu, L. Chen, Z. D. Chen, S. Li, *Nanoscale* **2019**, 11, 2871.

[13] a) G.E. Eperon, G.M. Paterno, R.J. Sutton, A. Zampetti, A.A. Haghighirad, F. Cacialli, H.J. Snaith, *J. Mater. Chem. A* **2015**, *3*, 19688-19695; b) L.A. Frolova, D.V. Anokhin, A.A. Piryazev, S.Y. Luchkin, N.N. Dremova, K.J. Stevenson, P.A. Troshin, *J. Phys. Chem. Lett.* **2017**, *8*, 67-72; c) C.-Y. Chen, H.-Y. Lin, K.-M.

Chiang, W.-L. Tsai, Y.-C. Huang, C.-S. Tsao, H.-W. Lin, *Adv. Mater.* **2017**, *29*, 1605290-n/a.

[14] a) F. Hao, C.C. Stoumpos, R.P.H. Chang, M.G. Kanatzidis, *J. Am. Chem. Soc.* **2014**, *136*, 8094-8099; b) Z. Yang, A. Rajagopal, C.-C. Chueh, S.B. Jo, B. Liu, T. Zhao, A.K.-Y. Jen, *Adv. Mater.* **2016**, *28*, 8990-8997.

[15] B. Han, B. Cai, Q. Shan, J. Song, J. Li, F. Zhang, J. Chen, T. Fang, Q. Ji, X. Xu, H. Zeng, *Adv. Func. Mater.* **2018**, *28*, 1804285.

[16] W. Travis, E. Glover, H. Bronstein, D. Scanlon, R. Palgrave, *Chem. Sci.* **2016**, *7*, 4548-4556.

[17] a) T.S. Sherkar, C. Momblona, L. Gil-Escrig, J. Ávila, M. Sessolo, H.J. Bolink, L.J.A. Koster, *ACS Energy Lett.* **2017**, *2*, 1214-1222; b) D. Moerman, G.E. Eperon, J.T. Precht, D.S. Ginger, *Chem. Mater.* **2017**, *29*, 5484-5492; c) Y. Yamada, T. Yamada, A. Shimazaki, A. Wakamiya, Y. Kanemitsu, *J. Phys. Chem. Lett.* **2016**, *7*, 1972-1977.

[18] a) Y. Dang, Y. Zhou, X. Liu, D. Ju, S. Xia, H. Xia, X. Tao, *Angew. Chem. Int. Edit.* **2016**, *55*, 3447-3450; b) Z. Zhu, C.-C. Chueh, N. Li, C. Mao, A.K.Y. Jen, *Adv. Mater.* **2018**, *30*, 1703800.

[19] a) N. Zhou, Y. Shen, L. Li, S. Tan, N. Liu, G. Zheng, Q. Chen, H. Zhou, *J. Am. Chem. Soc.* **2018**, *140*, 459-465; b) S. Shao, J. Liu, G. Portale, H.-H. Fang, G.R. Blake, G.H. ten Brink, L.J.A. Koster, M.A. Loi, *Adv. Energy Mater.* **2018**, *8*, 1702019; c) Q. Wang, X. Zheng, Y. Deng, J. Zhao, Z. Chen, J. Huang, *Joule* **2017**, *1*, 371-382; d) T. Zhang, M.I. Dar, G. Li, F. Xu, N. Guo, M. Grätzel, Y. Zhao, *Sci.*

Adv. **2017**, *3*, e1700841; e) Y. Liao, H. Liu, W. Zhou, D. Yang, Y. Shang, Z. Shi, B. Li, X. Jiang, L. Zhang, L.N. Quan, R. Quintero-Bermudez, B.R. Sutherland, Q. Mi, E.H. Sargent, Z. Ning, *J. Am. Chem. Soc.* **2017**, *139*, 6693-6699.

[20] a) D. Yu, F. Cao, Y. Shen, X. Liu, Y. Zhu, H. Zeng, *J. Phys. Chem. Lett.* **2017**, *8*, 2565-2572; b) D. Yu, B. Cai, F. Cao, X. Li, X. Liu, Y. Zhu, J. Ji, Y. Gu, H. Zeng, *Adv. Mater. Interfaces* **2017**, *4*, 1700441; c) D. Yu, F. Cao, Y. Gao, Y. Xiong, H. Zeng, *Adv. Func. Mater.* **2018**, *28*, 1800248.

[21] a) W. Chen, S. Xu, J.J. Day, D. Wang, M. Xian, *Angew. Chem. Int. Edit.* **2017**, *56*, 16611-16615; b) N. Cho, M. Shokeen, *J. Bone Oncol.* **2019**, *17*, 100249.

[22] J.R. Manders, T.-H. Lai, Y. An, W. Xu, J. Lee, D.Y. Kim, G. Bosman, F. So, *Adv. Func. Mater.* **2014**, *24*, 7205-7210.

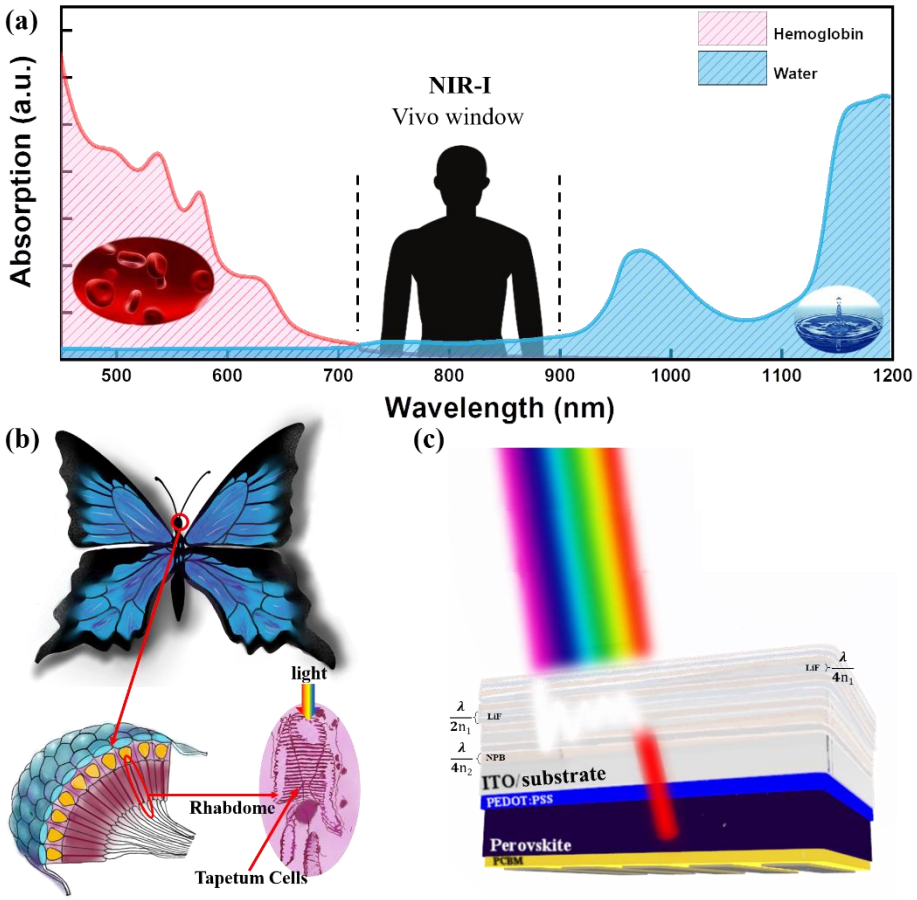

Figure 1. Constructing bionic PDs. a) Absorption spectra of hemoglobin and water (both are the basic component of human body). b) Schematic illustration of the micro structure of butterfly's ommatidium. c) Schematic illustration of the structure of bionic NIR PDs mimicking the morpho butterfly's ommatidium.

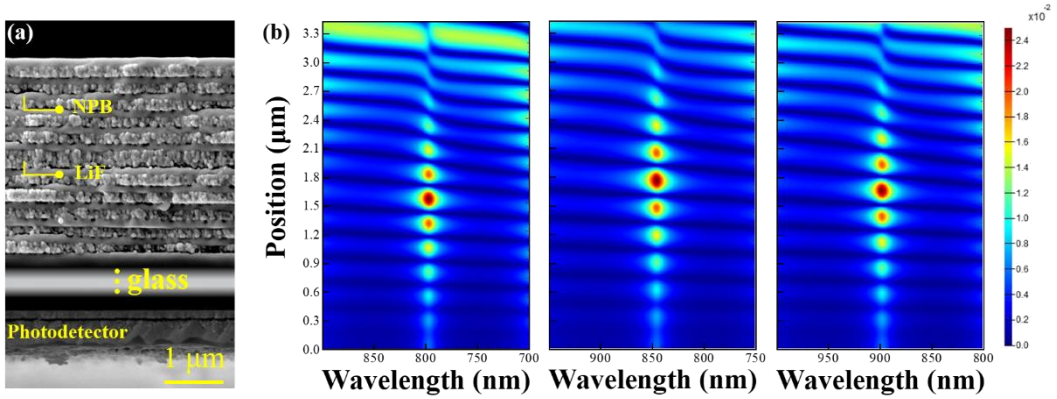

Figure 2. Bionic microcavities for selective light infiltration. a) Cross-section SEM images of the bionic optical microcavities. b) Simulation of the optical field distribution in the microcavities. The transmission peaks are at 800 nm, 850, and 900 nm respectively by tailoring of the thickness of dielectric media.

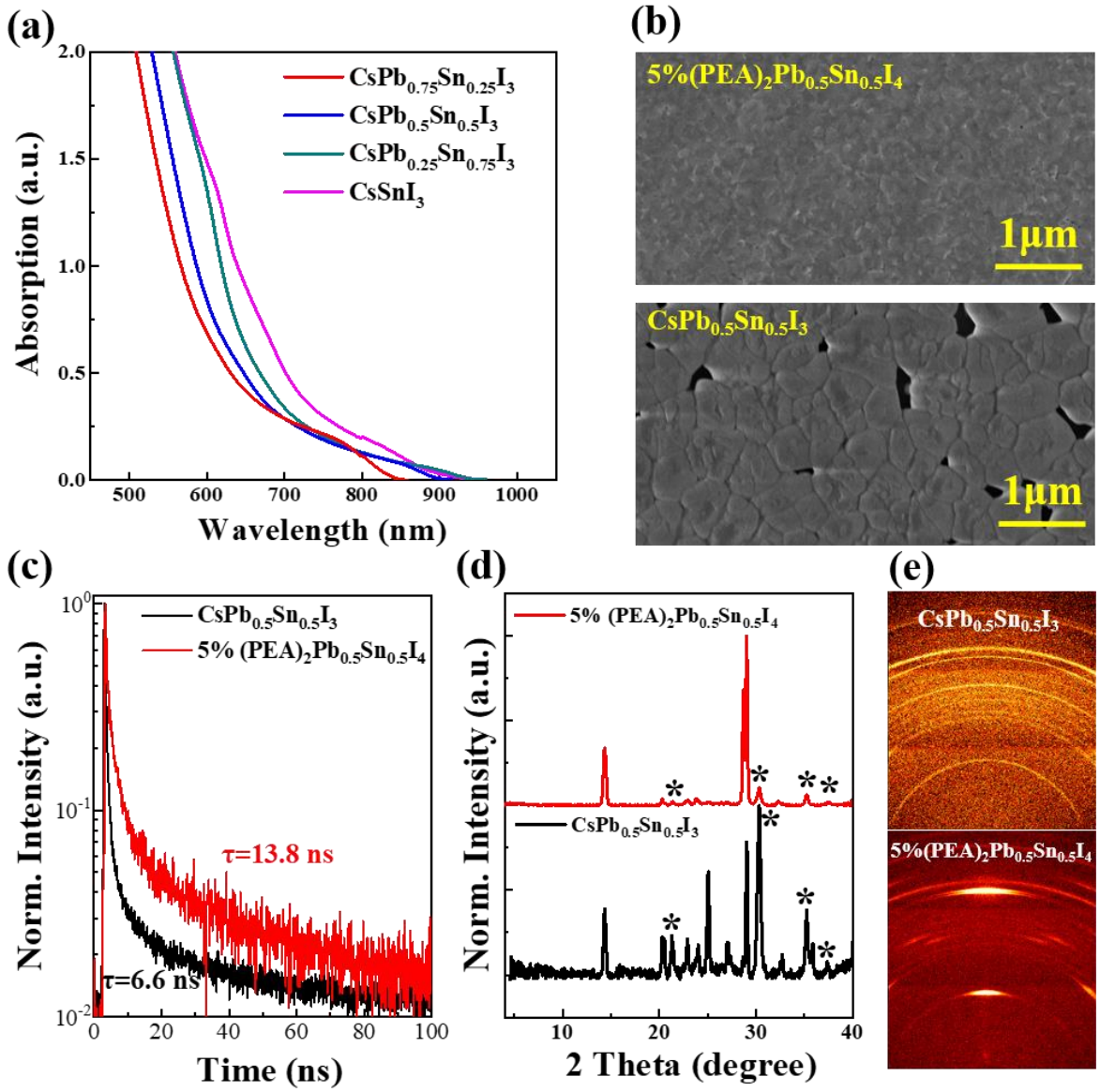

Figure 3. Composition and film engineering of the fully-inorganic HP film. a) UV-Vis absorption spectra of the HP film with different Pb/Sn ratios. b) Top view SEM images of the pristine $CsPb_{0.5}Sn_{0.5}I_3$ films and that with 5% 2D $PEA_2Pb_{0.5}Sn_{0.5}I_4$ additive. c) The PL decay transient spectra of the pristine $CsPb_{0.5}Sn_{0.5}I_3$ films and that with 5% 2D $PEA_2Pb_{0.5}Sn_{0.5}I_4$ additive. d) XRD and e) 2D XRD patterns of the pristine $CsPb_{0.5}Sn_{0.5}I_3$ films and that with 5% 2D $PEA_2Pb_{0.5}Sn_{0.5}I_4$ additive. * is the characteristic peak of glass substrate.

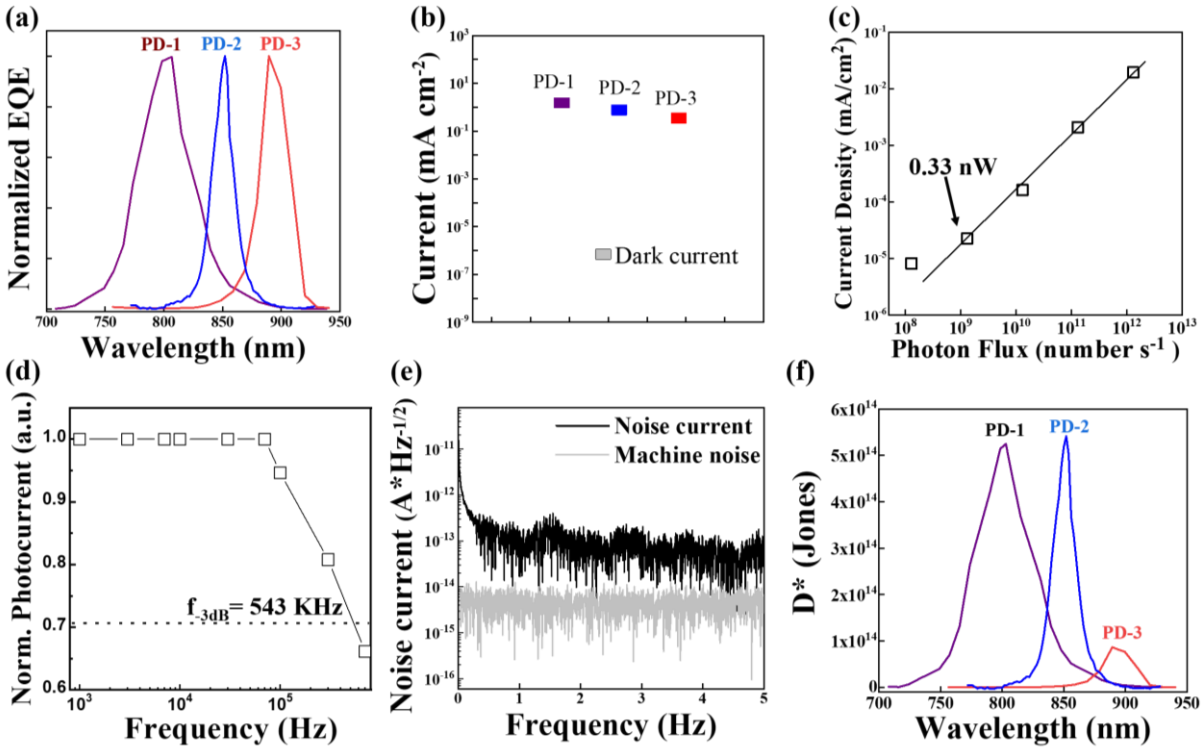

Figure 4. Characterizations of the bionic PDs. a) Normalized EQE spectra of the bionic NIR PDs with different transmission peaks. b) Dark current and photocurrent of the NIR-I PDs under flat-spectrum white light (AM 1.5 illumination) at shorted condition. c) LDR of the HP PDs under various light intensities. The solid line represents linear fitting. d) Normalized response loss versus light modulation frequency. e) Noise current extracted from Fourier transform of the dark current (monitored by Agilent A1500). f) Typical detectivity of NIR-I PDs with different transmission peaks.

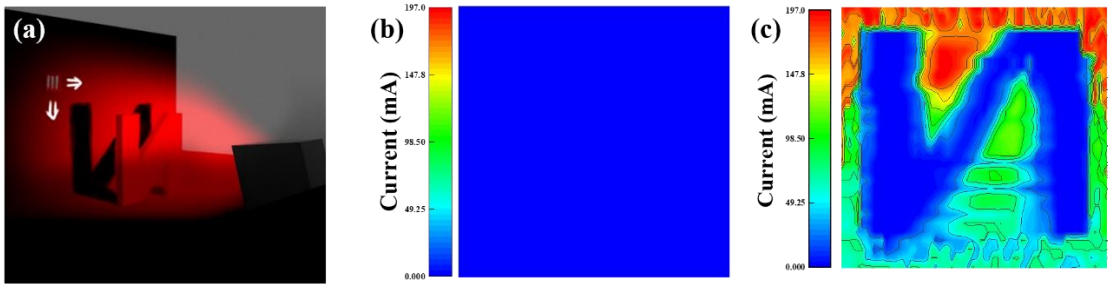

Figure 5. Proof-of-concept imaging of the PDs. a) Schematic illustration of the NIR imaging. And corresponding output images using the NIR- I PDs with peak response to 850 nm (PD-2) under b) 750 nm and c) 850 nm photon sources, respectively.

Bionic photodetectors with microcavities mimicking the compound eyes of butterfly are developed to realize selective light response in the NIR-I biological window. Inorganic halide perovskite with comprehensive composition and film engineering is adopted as the photoactive layer. The overall device affords superior performance for practical applications.

Keyword: Halide perovskite, bionic photodetector, NIR-I detection, narrowband detection, fluorescence imaging

Fei Cao,[#] Jingde Chen, [#] Dejian Yu, [#] Shu Wang, Xiaobao Xu, Jiaxin Liu, Zeyao Han, Bo Huang, Yu Gu, Haibo Zeng**

Bionic Detectors Based on Low-Bandgap Inorganic Perovskite for Selective NIR-I Photon Detection and Imaging